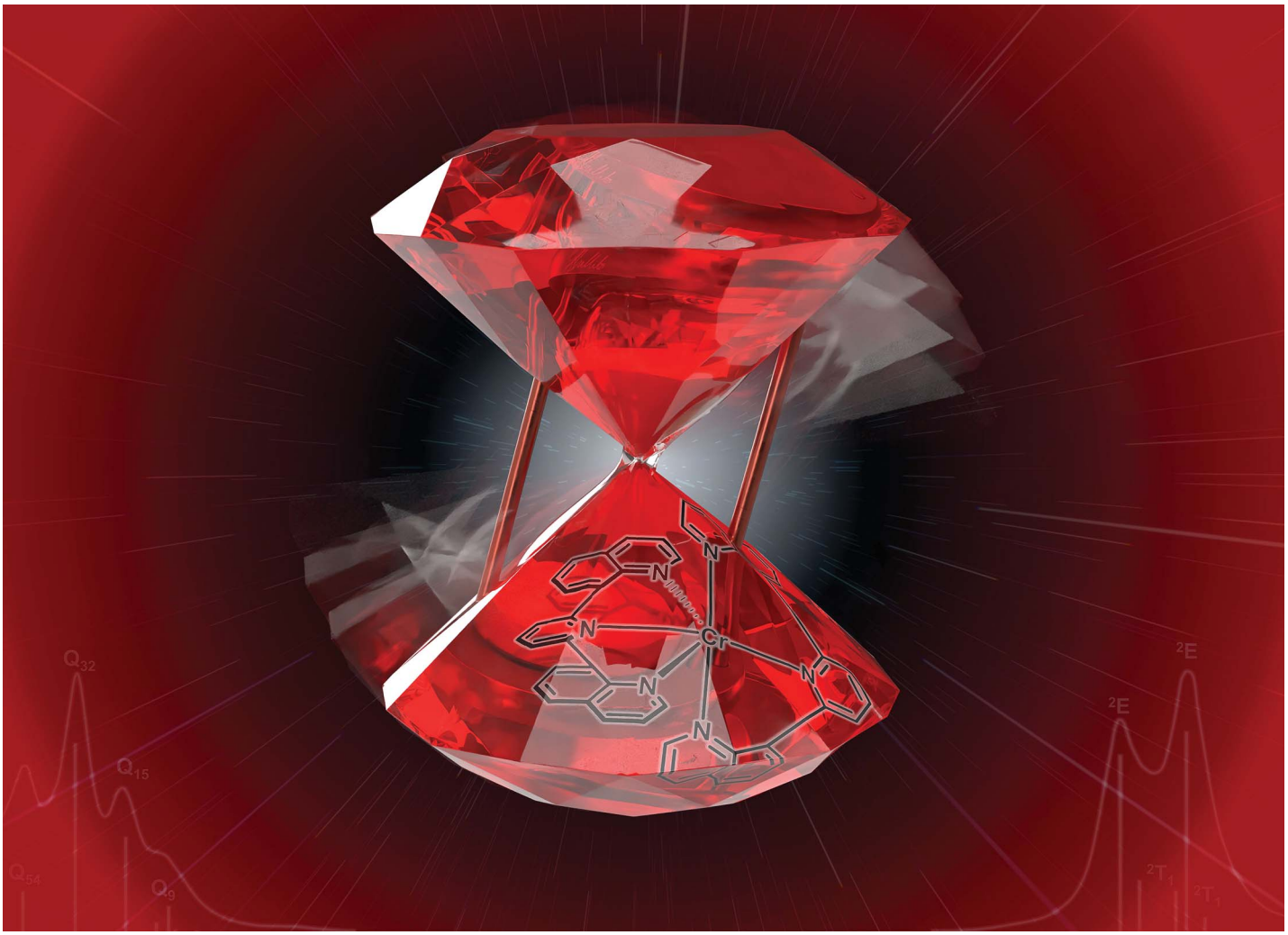

Showcasing research from Dr. Stephan Kupfer's laboratory, Institute of Physical Chemistry, Friedrich-Schiller-University Jena, Germany.

Unraveling the photoredox chemistry of a molecular ruby

In-depth computational modelling using state-of-the-art multiconfigurational methods allowed us to elucidate the photophysical processes as well as their kinetics in a Cr(III) spin-flip complex. Particular emphasis was set on investigating various intersystem crossing channels connecting the respective quartet and doublet spin states. Furthermore, ab initio molecular dynamics allowed us to evaluate the photoredox chemistry of the millisecond lived excited molecular ruby in combination with a reductive quencher.

Image reproduced by permission of Dr. Georgina E. Shillito and Dr. Stephan Kupfer from *Chem. Sci.*, 2025, **16**, 18113.

As featured in:

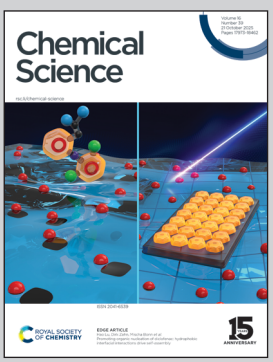

See Georgina E. Shillito, Stephan Kupfer *et al.*, *Chem. Sci.*, 2025, **16**, 18113.

ROYAL SOCIETY OF CHEMISTRY

15 YEARS ANNIVERSARY

rsc.li/chemical-science

Registered charity number: 207890

Chemical Science

ROYAL SOCIETY OF CHEMISTRY

EDGE ARTICLE

View Article Online
View Journal | View Issue

Cite this: *Chem. Sci.*, 2025, **16**, 18113

All publication charges for this article have been paid for by the Royal Society of Chemistry

Unraveling the photoredox chemistry of a molecular ruby

Guangjun Yang, [a] Georgina E. Shillito, [a] Phillip Seeber, [ab] Oliver S. Wenger [c] and Stephan Kupfer *[a]

In contrast to well-studied $4d^6$ and $5d^6$ transition metal complexes such as the modern-day drosophila of photochemistry, Ru(II)-tris(bipyridine), which often feature a typical triplet metal-to-ligand charge transfer emission in the nanosecond timescale, the photophysics of Cr(III) complexes are drastically different. The $3d^3$ configuration of the chromium(III) allows for an unusual spin-flip emission from the low-lying metal-centered (MC; $^2T_1$ and ^2E) states, exhibiting lifetimes up to the milliseconds to seconds timescale. In this fully computational contribution, the photophysical properties as well as the application of such long-lived excited states in the context of photoredox chemical transformations are investigated for the recently introduced $[Cr(dqp)_2]^{3+}$ [Cr(III)-(2,6-bis(8′-quinolinyl)pyridine)$_2$]$^{3+}$, otherwise known as a type of molecular ruby. Our in-depth theoretical characterization of the complicated electronic structure of this $3d^3$ system relies on state-of-the-art multiconfigurational methods, *i.e.* the restricted active space self-consistent field (RASSCF) method followed by second-order perturbation theory (RASPT2). This way, the light-driven processes associated with the initial absorption from the quartet ground state, intersystem crossing to the doublet manifold as well as the spin-flip emission were elucidated. Furthermore, the applicability of the long-lived excited state in $[Cr(dqp)_2]^{3+}$ in photoredox chemistry, *i.e.* reductive quenching by *N*,*N*-dimethylaniline, was investigated by *ab initio* molecular dynamics (AIMD). Finally, the thermodynamics and kinetics of these underlying intermolecular electron transfer processes were analyzed in the context of semiclassical Marcus theory.

Received 11th July 2025
Accepted 9th September 2025

DOI: 10.1039/d5sc05170c

rsc.li/chemical-science

1 Introduction

The conversion of solar energy directly into electricity and chemical fuels, such as hydrogen or hydrocarbons, stands as a primary goal for humankind in order to transform our energy sector towards sustainability. In recent decades, luminescent transition metal complexes have been thoroughly investigated and widely utilized across diverse fields.[1–8] Traditionally, there has been significant dependence on compounds containing 4d and 5d transition metals such as Ru(II), Ir(III), Os(II) or Pt(II).[9–23] The combination of favorable redox properties, efficient light-harvesting capabilities and stability to light, heat, and pH make them desirable candidates for light-harvesting or (photo) catalytic processes. Furthermore, on account of the large t_{2g}–e_g ligand field splitting in octahedral 4d and 5d polypyridyl complexes and heavy-atom facilitated spin–orbit coupling (SOC), the lowest energy excited state is often emissive, long-lived and of triplet metal-to-ligand charge transfer (^{3}MLCT) character. Metal centered (MC) states, whose population typically results in rapid non-radiative deactivation to the ground state and potentially even photodegradation, are high in energy and usually not easily accessible. In contrast the excited states of polypyridyl complexes of 3d metals such as Fe(II) and Co(III) are normally short-lived and non-emissive,[24–28] due to low-lying and rapidly accessible MC states. Electronically, this drastically altered situation stems from the primogenic effect, *i.e.*, the smaller overlap of the 3d-orbitals with the ligand's lone-pair orbitals.[29]

In contrast certain, carefully designed Cr(III) complexes – with a quartet $3d^3$ ground state configuration – are often strongly emissive and can exhibit unusually long excited state lifetimes. This behavior is attributed to a property known as spin-flip emission.[5,30–32] In the case of this curious phenomenon, the excited state and the ground state share the same electronic configuration, with the only difference being the spin of one electron, see Fig. 1A.

In the case of the present Cr(III)-based family of complexes (see $[Cr(dqp)_2]^{3+}$ as shown in Fig. 1B), this unique electronic structure leads to phosphorescence from a ^{2}MC state back to the ^{4}MC ground state. These emissive states are in stark contrast to the common emissive ^{3}MLCT states, *i.e.* in second- and third-row transition metal coordination compounds with

[a]*Institute of Physical Chemistry, Friedrich Schiller University Jena, Lessingstraße 4, 07743 Jena, Germany*

[b]*University Computer Centre, Friedrich Schiller University Jena, Am Johannesfriedhof 2, 07743 Jena, Germany*

[c]*Department of Chemistry, University of Basel, St. Johanns-Ring 19, 4056 Basel, Switzerland. E-mail: stephan.kupfer@uni-jena.de*

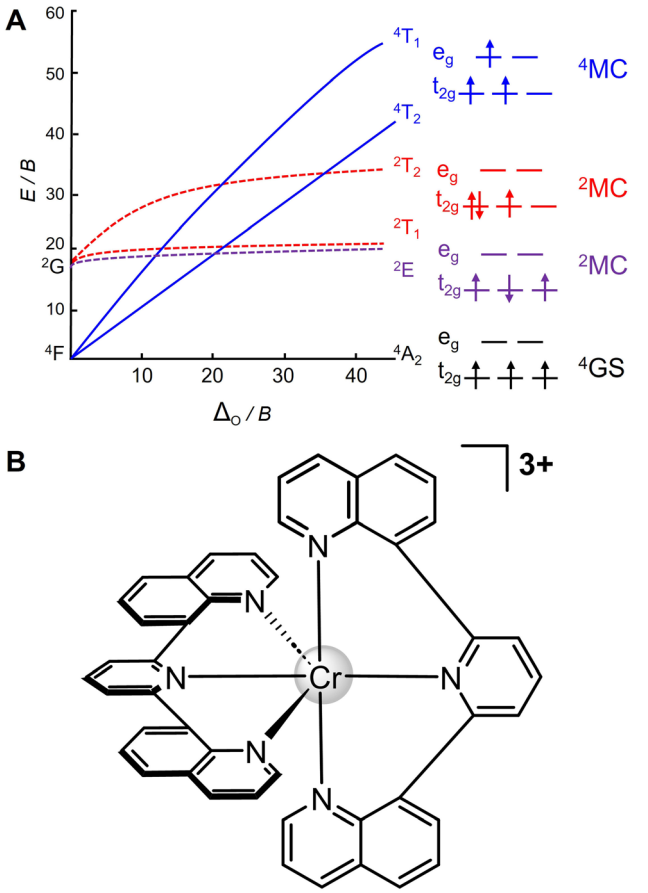

Fig. 1 (A) Tanabe–Sugano diagram of d^3 octahedral ligand field and, (B) structure of $[Cr(dqp)_2]^{3+}$.

e.g., d^6 and d^8 configurations. Notably, traditional ligands such as 1,2-ethylenediamine (en) or 2,2′;6′,2″-terpyridine (tpy) are not suited to rationalize spin-flip luminescence in $3d^3$ systems, such as Cr(III),[33,34] due to their substantial divergence from a perfectly octahedral geometry (by approximately 7° to 11°). In consequence, a relatively weak ligand field is formed based on the inefficient overlap of the respective orbitals forming the coordination environment. Thus, the proximity of the ^{4}MC excited state ($^4T_2$) and ^{2}MC states (^2E and $^2T_1$), as shown in Fig. 1A, promotes back-intersystem crossing (bISC) from the $^2E/^2T_1$ states to the Jahn–Teller distorted $^4T_2$ states. This process is known to reduce the excited state lifetime by population of undesirable pathways associated with non-radiative decay or even (photo)degradation of the coordination environment.[30,35] Therefore, the pursuit of enhancing ligand field splitting by judicious ligand selection to construct a perfectly octahedral structure has become a focal point of interest for synthetic and theoretical chemists in the past ten years.[31,34,36–45] For instance, the Heinze group recently reported the coordination of two six-membered 2,6-bis(2-pyridylmethyl)pyridine (bpmp) and *N*,*N*′-dimethyl-*N*,*N*′-dipyridine-2-ylpyridine-2,6-diamine (ddpd) chelates ($[Cr(bpmp)_2]^{3+}$ and $[Cr(ddpd)_2]^{3+}$). The careful ligand selection not only provides less distorted excited states, thereby limiting the non-radiative decay but also strong ligand field splitting to prevent undesirable $^4T_2$–$^2E/^2T_1$ bISC. Both Cr(III) complexes display significantly long lifetimes (bpmp: 1360 μs; ddpd: 889 μs) and high luminescence quantum yields (bpmp: 12.3%; ddpd: 11.0%) in deaerated aqueous solutions at room temperature.[39,45] Notably, the nuclear charge of the central metal (ion) is key to balancing the energy levels of the involved locally excited MC states and charge transfer states. As suggested by recent studies on several $3d^3$ complexes, Cr(III) seems to represent a unique sweet spot in the periodic table of elements which facilitates population of rather low-lying $^{4/2}$MC states involved in the spin-flip-based lifetime elongation. In contrast, introduction of V(II) and Mn(IV) centers – with a comparable $3d^3$ configuration –alters the complex excited state landscape in favor of MLCT and LMCT (ligand-to-metal charge transfer) processes, respectively.[32,46–48]

In the present contribution, we carefully evaluate the photophysical and photoredox properties associated with spin-flip luminescence of a Cr(III) complex [Cr(III)-(2,6-bis(8′-quinolinyl) pyridine)$_2$]$^{3+}$ ($[Cr(dqp)_2]^{3+}$), see Fig. 1B, which was first reported by Piguet's team in 2019.[41] Since then, this Cr(III) spin-flip system, which features an excited state lifetime of 1.2 ms (in water) at room temperature, was investigated in the context of developing material capable of circularly polarized luminescence in the near-infrared (NIR) region and polarized photonic devices based on earth-abundant metals.[41] Very recently, the photoredox properties of this long-lived spin-flip species in combination with a *N*,*N*-dimethylaniline (DMA) electron donor were investigated in the Wenger group.[36,49] Based on these previous works, the focus of the present contribution is set on unraveling the unique photophysical properties of Cr(III) spin-flip complexes and their application in light-driven redox chemistry by means of theoretical modelling with $\mathbf{[Cr(dqp)_2]^{3+}}$ as a representative complex for the molecular ruby family of compounds.

In order to provide an unbiased description of the involved electronic states, such as the ^{4}MC and ^{2}MC states of interest (as well as MLCT and LMCT states), multiconfigurational methods are necessary, which allow for the consideration of static electron correlation, particularly associated with the d-orbitals. Here, we utilize the state-of-the-art restricted active space self-consistent field (RASSCF) method followed by second-order perturbation theory (RASPT2). This methodology (RASPT2//RASSCF) allows for an elaborate description of both static and dynamic electron correlation for medium-sized coordination compounds.[50–52] In particular, splitting of the active space into three subspaces enables the construction of sizable active spaces which further accounts for addressing the double d-shell effect – related to the partial contribution of energetically close-lying 4d orbitals. In addition to modelling of the light-driven processes, we also estimate the kinetics of intersystem crossing (ISC) as well as emissive processes among the quartet and doublet states of interest. Furthermore, these demanding multiconfigurational calculations are compared to cost-efficient density functional and time-dependent density functional theory simulations (DFT and TDDFT). Surprisingly, the complex electronic structure of $\mathbf{[Cr(dqp)_2]^{3+}}$ within the quartet ground state as well as involving weakly dipole-allowed MC and strongly

dipole-allowed LMCT transitions are sufficiently described by cost-efficient TDDFT simulations as benchmarked with respect to RASPT2 and experimental reference data. Finally, the photoredox processes between the excited Cr(III) chromophore and a DMA electron donor are unraveled at the molecular level, *i.e.* associated with the thermodynamics and the kinetics of the intermolecular electron transfer reaction. To this aim, we rely on *ab initio* molecular dynamics (AIMD) to describe the light-driven electron transfer kinetics in the frame of semi-classical Marcus theory. Based on our AIMD simulations and subsequent Marcus analysis, a comparably fast intermolecular electron transfer from the DMA donor to the excited $[Cr(dqp)_2]^{3+}$ was determined, while the reduction of the molecular ruby involves partial reduction of the chromium as well as of the ligand sphere.

2 Computational details

The DFT and TDDFT calculations addressing structural and electronic properties in both the ground and excited state of $[Cr(dqp)_2]^{3+}$ were performed utilizing the Gaussian 16 program[53] with the B3LYP[54–59] exchange correlation (XC) functional. All multiconfigurational (RASPT2//RASSCF) calculations were performed in MOLCAS 8.4 (ref. 60) using the geometry (D_2 point group) as obtained at the DFT level of theory. AIMD simulations were performed using the CP2K 2024.1 software[61,62] to assess the intermolecular ET processes in solution (acetonitrile, DMA) in a fully periodic fashion using the BLYP functional.[55,57,63] A detailed description of the applied computational protocols is provided in the SI.

3 Results and discussion

3.1 Initial photoactivation

The DFT optimization of $[Cr(dqp)_2]^{3+}$ yields a D_2 structure with a quartet ground state ($^4A_2$, Fig. 1A). The spin density which allows the unpaired electron density to be visualized (Fig. 2D) reveals a $(t_{2g})^3$ electronic configuration, *i.e.* a quartet metal-centered (^{4}MC) ground state where the $3d_{xy}$, $3d_{xz}$ and $3d_{yz}$ orbitals are each singly occupied.[36,45,64] Notably, we apply in the following the typically utilized nomenclature to label the respective electronic states involved in the photophysics of pseudo-octahedral Cr(III) complexes, which stems from the O_h point group. The previously reported UV-vis absorption spectrum of $[Cr(dqp)_2]^{3+}$ in acetonitrile (AcN) features the typical absorptions at 335 and 377 nm as well as a weak shoulder tailing to 450 nm.[36] Analogously to the experiment, the electronic absorption spectrum of $[Cr(dqp)_2]^{3+}$, as obtained at the TDDFT level of theory and in AcN (polarizable continuum model), is dominated by two strongly dipole-allowed quartet ligand-to-metal charge transfer (^{4}LMCT) excitations (Q_{15} and Q_{32}), see Fig. 2A. In order to assign the nature of the respective

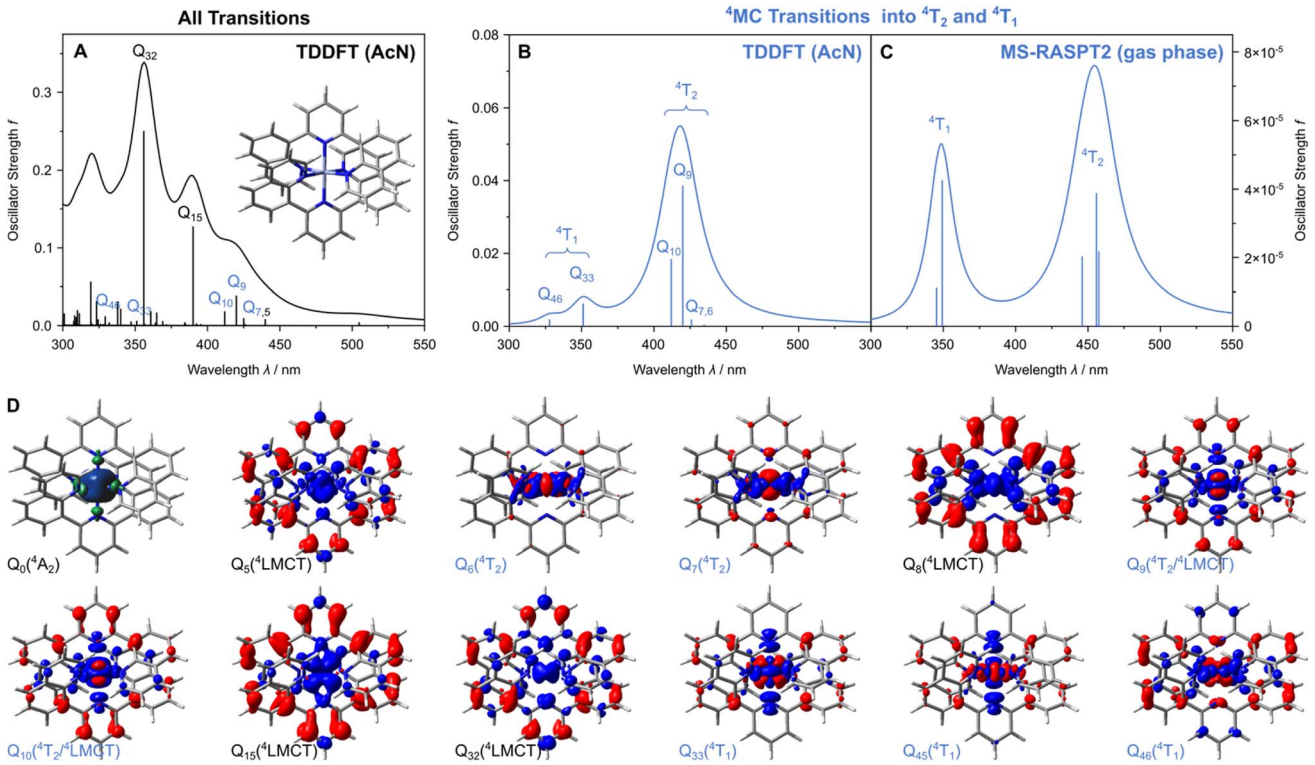

Fig. 2 (A) Simulated UV-vis absorption spectrum of $[Cr(dqp)_2]^{3+}$ as predicted at the TDDFT level of theory in acetonitrile (AcN). Simulated transitions are broadened by Lorentzian functions with a full width at half maximum of 0.1 eV; state labels according to color scheme of Fig. 1. (B) and (C) Contribution of quartet metal-centered (^{4}MC) transitions, *i.e.*, associated with low-energy $^4T_2$ and high-energy $^4T_1$ states at the TDDFT and MS-RASPT2 levels of theory, respectively. (D) Spin density of the quartet ground state ($^4A_2$) as well as charge density difference plots for selected ^{4}LMCT and ^{4}MC ($^4T_2$ and $^4T_1$) transitions; charge transfer occurs from red to blue.

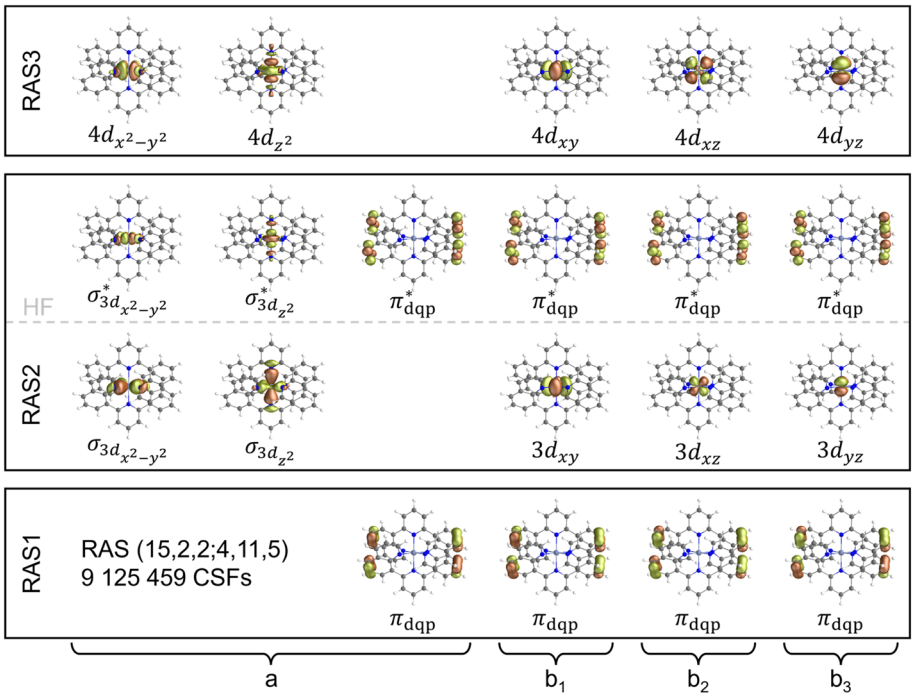

Fig. 3 Molecular orbitals for the RAS (15,2,2;4,11,5) used in the state average procedure covering the lowest eight quartet and the lowest eight doublet roots of $[Cr(dqp)_2]^{3+}$; two in each irreducible representation. The partitioning with respect to the RAS1, RAS2 and RAS3 subspaces is indicated as well as the orbital occupation within the Hartree–Fock (HF) reference wavefunction with each t_{2g} orbital being singly occupied within the quartet ground state. The active space spans over 9 125 459 configuration state functions (CSFs).

electronic transitions we utilize charge density difference plots, this approach provides a straightforward tool to visualize changes of electron density upon excitation, *i.e.* electron hole and excited electron, in a single picture, see Fig. 2D. These excitations involve a population transfer mainly from the high-lying π_{dqp} orbitals of both dqp ligands into the t_{2g} orbitals ($3d_{xy}$, $3d_{xz}$ and $3d_{yz}$). The predicted excitation energies of 3.18 and 3.48 eV (390 and 356 nm) are in good agreement with the experimental results (see Fig. 2A and Table S3). In addition, weakly-dipole allowed transitions associated with the $^4T_1$ states (excited ^{4}MC species) are predicted at 351 and 328 nm (Q_{33} and Q_{46}). Finally, TDDFT predicts two pure $^4T_2$ (^{4}MC) states (into Q_6 and Q_7) as well as two mixed states stemming from a linear combination of the third $^4T_2$ state and one ^{4}LMCT state (into Q_9 and Q_{10}). The excitation wavelengths of these $^4A_2 \rightarrow {}^4T_2$-transitions, ranging from 435 to 412 nm (Fig. 2 and Table S3), are in good agreement with the weak shoulder near 450 nm observed in the experimental UV-vis absorption spectrum.[36] Notably, this superposition of $^4T_2$ and ^{4}LMCT character was also reported by the Heinze group for $[Cr(bpmp)_2]^{3+}$ and $[Cr(ddpd)_2]^{3+}$.[39,65]

In the following, we benchmark these TDDFT simulations against our multi-state RASPT2 results as obtained by a restricted active space (15,2,2;4,11,5). This active space spans over more than 9 million configuration state functions (CFSs) and comprises of two pairs of σ/σ^* orbitals stemming from the linear combinations of the e_g orbitals ($3d_{x^2-y^2}$ and $3d_{z^2}$) and the respective lone-pairs of the two dqp ligands, the three t_{2g} orbitals ($3d_{xy}$, $3d_{xz}$ and $3d_{yz}$), four pairs of π_{dqp}/π^*_{dqp} orbitals as well as the five 4d orbitals to account for the double d-shell effect, see Fig. 3. RASPT2 simulations were performed in quartet and doublet multiplicity to address the relevant ^{4}LMCT, ^{4}ILCT, ^{4}MC states and ^{2}MC states (Tables S4 and S5); see SI for details regarding the computational setup.

Consistent with the DFT picture, the electronic ground state exhibits a $^4A_2$ character (see Table S4), which features surprisingly a rather small multiconfigurational character as given by the reference weight of 86% for the Hartree–Fock determinate. Furthermore, three low-lying ^{4}MC ($^4T_2$) states are predicted at 2.71, 2.72 and 2.78 eV (457, 456 and 446 nm), respectively. The weakly dipole-allowed excitations into these ^{4}MC states are in excellent agreement with the experimentally observed shoulder at approximately 450 nm. The higher energy $^4T_1$ (^{4}MC) state also splits into three energy levels based on the pseudo-octahedral D_2 symmetry. Energetically, the weakly dipole-allowed excitations are almost degenerate, at 349 and 345 nm (3.55 and 3.59 eV), while another excitation at slightly higher energy is dipole-forbidden (at 3.83 eV, 324 nm), see Fig. 2C and Table S4. Finally, the lowest energy ^{4}ILCT state is obtained at 299 nm (4.14 eV); notably, this state features significant contributions of double excitations (DE), which are not covered by the TDDFT scheme, see Fig. S2c and Table S4.

Comparison of the multiconfigurational results for the low-lying $^4T_2$ as well as for the higher lying $^4T_1$ states with the TDDFT results reveals that, surprisingly, the B3LYP functional provides a balanced description of the electronic transitions associated with the ^{4}MC states of interest. In case of the three $^4T_2$ states, MS-RASPT2 predicts excitation energies of 2.71, 2.72 and 2.78 eV, while the TD-B3LYP energies are slightly

overestimated by 0.04–0.1 eV (gas phase: 2.81, 2.88 and 2.92 eV, Table S2). In a similar fashion, the TDDFT and RASPT2 predicted $^4T_1$ energies are in very good agreement (3.49, 3.74 and 3.75 eV *vs.* 3.55, 3.59 and 3.83 eV, Table S2). Noteworthily, the energy levels of these metal-centered states are (almost) insensitive to the solvent environment (AcN, Table S3). Therefore, and in summary, both TDDFT and MS-RASPT2 provide a balanced description of the energetics of the (quartet) ligand field states in **[Cr(dqp)$_2$]$^{3+}$**.

3.2 Intersystem crossing channels and spin-flip emission

In the following section, we evaluate the kinetics of the ISC channels from the ^{4}MC excited states ($^4T_2$) to the energetically close lying ^{2}MC states (*i.e.* $^2T_2$, $^2T_1$ and ^2E) and the relaxation processes associated with the spin luminescence. Typically ISC in transition metal complexes occurs within few picoseconds or even on the sub-picosecond timescale based on pronounced relativistic effects introduced by the central metal atom (or other heavy atoms in the ligands sphere).[66–68] The present Cr(III) complex features a quartet ground state ($^4A_2$) and the initially populated excited states upon irradiation in the visible region are of $^4T_2$ character, as discussed in Section 3.1. In addition to these quartet states, MS-RASPT2 was also utilized to investigate the low-lying doublet states of **[Cr(dqp)$_2$]$^{3+}$**. Notably, the equilibrium structures of the quartet ground state and of the emissive spin-flip doublet state are almost identical.[36] Thus, the doublet energy levels, spin–orbit couplings (SOCs) and relaxation kinetics are obtained exclusively within the Franck–Condon region ($^4A_2$ ground state structure). The RASPT2 picture, predicted for the doublet (^{2}MC) states, is consistent with the Tanabe–Sugano diagram, see Fig. 1A and Table S5. Two ^2E states are predicted at 2.03 and 2.11 eV (611 and 588 nm), which are energetically close to the three predicted $^2T_1$ states at 2.00, 2.04 and 2.08 eV (620, 608 and 596 nm), respectively.

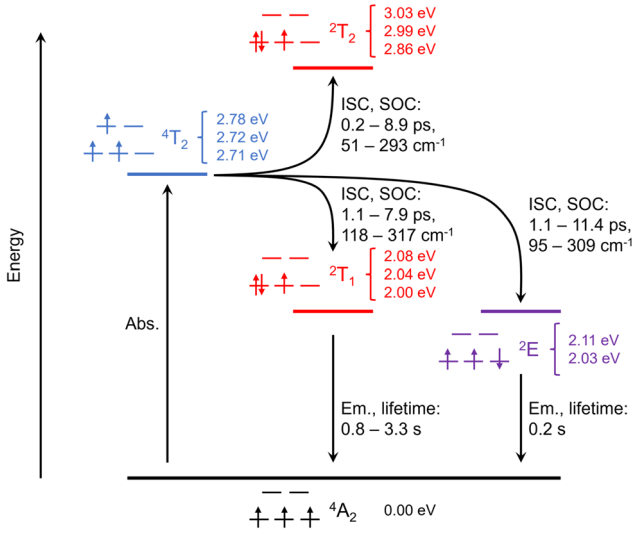

Fig. 4 Jablonski scheme visualizing excited state processes in [Cr(dqp)$_2$]$^{3+}$ associated with intersystem crossing (ISC) from the quartet to the doublet manifold and radiative phosphorescence lifetimes as obtained based on the multiconfigurational results.

Furthermore, the three $^2T_2$ states are found slightly higher in energy, *i.e.*, at 2.86, 2.99 and 3.03 eV (434, 415, 409 nm), respectively, see Fig. 4.

To treat both relativistic effects and electron correlation, the exact spin-free (SF) components and spin-dependent first-order Douglas–Kroll–Hess Hamiltonian[69] are combined to calculate the spin–orbit couplings (SOCs) among the states of interest at the MS-RASPT2 level of theory. This way, spin–orbit (SO) states are constructed as linear combinations based on the individual SF states – the respective electronic states of quartet and doublet multiplicity. Thereby, the mixing between the otherwise orthogonal SF quartet and doublet states is reflected by their SOC, *i.e.* $\langle Q_j|\hat{H}_{SOC}|D_i\rangle$. The electronic absorption spectrum related to the $^{4/2}$MC states of interest within the SO picture (Fig. S3) is almost identical to the SF representation as shown in Fig. 2C. In order to evaluate the rate of ISC, the energies as well as the SOCs among the involved quartet and doublet states are essential; herein, we focus on the SOCs between the low-lying ^{4}MC and ^{2}MC states associated with the spin-flip of interest. Since the $^4T_1$ states are less stable than the $^4T_2$ states and undergo rapid internal conversion (IC) to the $^4T_2$ states and subsequent vibrational cooling within 1–10 ps,[70] ISC from the high-energy $^4T_1$ states (3.55–3.83 eV, Table S4) is not considered in the present study.

In the case of **[Cr(dqp)$_2$]$^{3+}$** our computational results reveal that the $^4T_2$ states are strongly coupled with the low-lying $^2T_1$ and ^2E states (95–317 cm^{-1}) as well as the higher-lying $^2T_2$ states (51–293 cm^{-1}). In comparison to other 3d transition metal complexes, the magnitude of these SOCs is rather large, which reflects the metal-centered character of the quartet donor and doublet acceptor states. Based on the energies and the SOCs among the $^{4/2}$MC states, ISC rates were obtained for both energetically uphill ($^4T_2 \rightarrow {}^2T_2$) and downhill ($^4T_2 \rightarrow {}^2T_1$ and $^4T_2 \rightarrow {}^2E$) processes, see eqn (1) and (2) in the SI. As shown in Fig. 4, in all cases considered herein, ultrafast ISC proceeds with rate constants in the range of 10^{11} to 10^{12} s^{-1} (0.2 to 11.4 ps), see Table 1 for details. These computational results clearly show that all ^{2}MC states ($^2T_2$, $^2T_1$ and ^2E) are rapidly accessible upon ISC from the $^4T_2$ states. Subsequently, internal conversion proceeds which leads presumably to an equal population of the quasi isoenergetic $^2T_1$ and ^2E states.

The constructed Jablonski diagram (Fig. 4) indicates that the coordination of the dqp ligands to the metal is associated with an almost ideal overlap between e_g orbitals and the lone-pairs of the ligands, which is reflected by the almost perfect octahedral geometry (see bite angles in Table S1). This way, a strong ligand field splitting, which raises the $^4T_2$ states far above the ^2E and $^2T_1$ states is established. Thermodynamically, the population of $^2T_1$ and ^2E states is most favorable with driving forces of approximately −0.7 eV. This way, bISC to the quartet states ($^4T_2$) is hampered, which leads to an enhanced phosphorescence quantum yield.

Finally, the population of the emissive $^2E/^2T_1$ states enables radiative decay (k_P) to the (quartet, $^4A_2$) ground state – or more precisely emission based on the energies and transition dipole moments between the respective SO states. As ISC to the $^2T_1$ (1.1–7.9 ps) and ^2E states (1.1–11.4 ps) occurs at almost identical

Table 1 Calculated ISC rate constants (top, in $s^{-1} \times 10^{11}$) as well as spin–orbit coupling elements $\langle Q_j|\hat{H}_{SOC}|D_i\rangle$ (bottom and in parenthesis, in cm^{-1}), between prominent excited quartet and doublet states of $[Cr(dqp)_2]^{3+}$. All results were obtained at the RASPT2 level of theory

SOC k_{ISC}	$^2T_1$ (2.00 eV)	^2E (2.03 eV)	$^2T_1$ (2.04 eV)	$^2T_1$ (2.08 eV)	^2E (2.11 eV)	$^2T_2$ (2.86 eV)	$^2T_2$ (2.99 eV)	$^2T_2$ (3.03 eV)
$^4T_2$ (2.71 eV)	0 (0)	9.46 (309)	2.51 (158)	1.60 (118)	2.81 (149)	18.12 (113)	12.61 (154)	0 (0)
$^4T_2$ (2.72 eV)	9.01 (317)	0.87 (95)	1.56 (126)	0 (0)	5.76 (216)	32.60 (146)	0 (0)	1.13 (51)
$^4T_2$ (2.78 eV)	1.27 (128)	1.58 (138)	0 (0)	3.58 (194)	5.55 (231)	0 (0)	16.30 (140)	53.30 (293)

timescales, a Boltzmann distribution of the respective microstates is expected. In consequence, the simulated emission spectrum is comprised of contributions from all three $^2T_1$ and both ^2E states. However, the Boltzmann population of the respective ^2E and $^2T_1$ states was approximated to be equal among the five quasi-isoenergetic microstates. This simplification was employed as no state-specific relaxation was performed, which would be essential to obtain reliable Boltzmann factors for each state, respectively. As shown in Fig. 5, two close-lying emissions bands at 609 and 588 nm (see Fig. 5), which are mainly associated with "true" spin-flip emission ($^2E \rightarrow {}^4A_g$) emission at 611 and 588 nm (at 2.03 and 2.11 eV).

Emission from the $^2T_1$ states (at 596, 609 and 620 nm, 2.00, 2.04, 2.08 eV) is less prominent due to their small transition dipole moments (see eqn (3) in the SI). This finding is also reflected by the calculated radiative lifetimes of 0.2 s in the case of the ^2E states and even and 0.8–3.2 s for the $^2T_1$ states, see Table 2. These computational results are in reasonable agreement with the experimentally observed emission of $[Cr(dqp)_2]^{3+}$, which features two narrow emission bands at 747 and 724 nm (1.66 and 1.71 eV), which were assigned to the lowest energy ^2E and $^2T_1$ states, respectively.[36,41] We attribute the overestimation of the simulated emission energies (roughly +0.35 eV) mainly to the lack of excited state structural relaxation within our computational approach. In slight contrast to the previous assignment, our scalar relativistic MS-RASPT2 simulations suggest that both emission bands are related to ^2E states, *i.e.*, due to their larger transition dipole moments (to the quartet ground state) as well as based on their shorter excited state lifetimes (see Fig. 4 and Table 2).

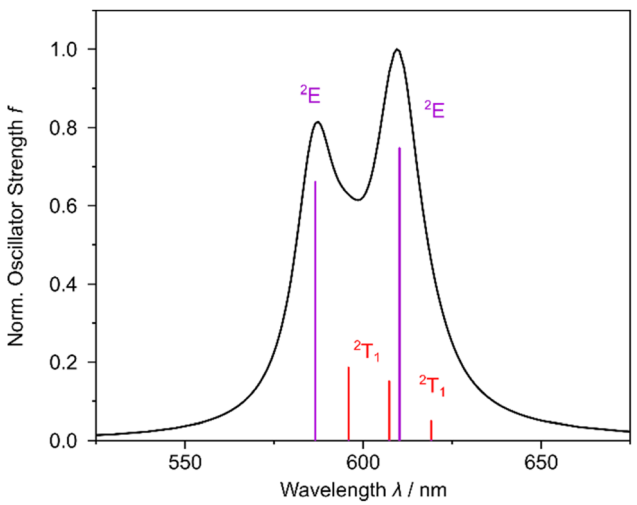

Fig. 5 Simulated emission spectrum of $[Cr(dqp)_2]^{3+}$ based on the MS-RASPT2 data.

Table 2 Simulated radiative phosphorescence rates k_P (s^{-1}) between low-lying doublet excited states (^2E and $^2T_1$) and the quartet ground state of $[Cr(dqp)_2]^{3+}$ and associated radiative lifetimes ($\tau_{Rad} = 1/k_P$ in s)

	$^2T_1$ (2.00 eV)	^2E (2.03 eV)	$^2T_1$ (2.04 eV)	$^2T_1$ (2.08 eV)	^2E (2.11 eV)
k_P	0.31	4.80	1.25	0.98	4.59
$1/k_P$	3.28	0.21	0.80	1.02	0.22

3.3 Intermolecular electron transfer

Based on our in-depth quantum chemical simulations, which allowed us to unravel the light-driven intramolecular processes and the spin-flip emission of the present molecular ruby system, we aim to extend our understanding in the context of its photoredox chemistry, *i.e.*, in the presence of a reductive quencher. Previously, Wenger *et al.* provided valuable insights into the driving force dependence of photoinduced ET between $[Cr(dqp)_2]^{3+}$ and a series of electron donors.[36,71] The quenching rate was investigated through Stern–Volmer kinetics, using time-resolved luminescence and UV-vis transient absorption spectroscopy. Building on these recent studies, our quantum chemical and *ab initio* molecular dynamics (AIMD) simulations enable us to derive detailed structure–property relationships with respect to the underlying intermolecular electron transfer processes between the spin-flip excited Cr(III) complex and the electron donor in solution (AcN). Here, we focus our computational efforts exclusively on the reductive quenching by *N*,*N*-dimethylaniline (DMA) as a representative organic electron donor. The derived theoretical understanding of the thermodynamic and kinetic properties is crucial to harvest the energy of millisecond-lived excited states in Cr(III) spin-flip complexes in future photocatalytic applications.

In order to investigate the ET kinetics between an excited $[Cr(dqp)_2]^{3+}$ (^2E or $^2T_1$ states) and DMA in AcN, we rely on *ab initio* molecular dynamics in combination with a QM/MM (quantum mechanical/molecular mechanical) approach. Thereby, the reactants – one $[Cr(dqp)_2]^{3+}$ complex as well as one DMA molecule – as well as the first solvent shell (31 AcN molecules) and respective counter ions are described quantum mechanically within a 30 × 22 × 22 $Å^3$ box using density functional theory (BLYP with DZVP-MOLOPT-SR-GTH basis sets and D3BJ dispersion correction).[55,57,72–74] As visualized in Fig. 6A, this QM system is embedded in a MM box of 59.7 × 47.7 × 52.1

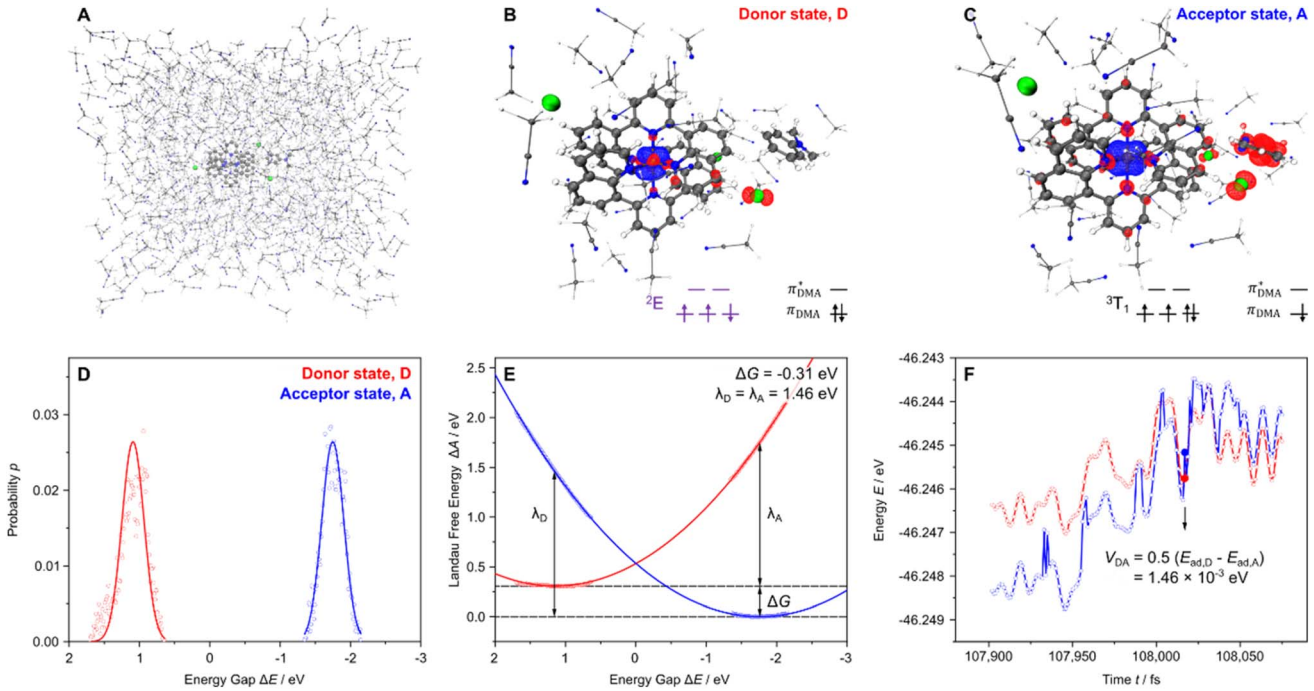

Fig. 6 (A) AIMD setup with one $[Cr(dqp)_2]^{3+}$ complex, one DMA molecule, three chloride ions and 31 AcN solvent molecules in the QM box (30 × 22 × 22 Å^3), embedded in a MM box (59.7 × 47.7 × 52.1 Å^3), which contains further 729 solvent molecules. (B) and (C) Spin density of QM region within the donor and the acceptor state respectively; blue and red represents α and β-spin, respectively. (D) Probability (dots) of the various energy gaps ΔE of the donor (red) and the acceptor state (blue) states along the trajectory as well as ideal Gaussian distributions; bin size is 1 kJ mol^{-1}. (E) Fitted Marcus parabolas of the donor and acceptor states using the Warshel histogram approach; driving force and reorganization energies are indicated. (F) Intersection region of the diabatic potential energy curves along the trajectory and electronic coupling obtained by the minimum energy splitting method.

Å^3 containing additional 729 solvent molecules as described using the GAFF2 force field ($T = 100$ K).[75–78] Further details with respect to the computational setup are summarized in the SI.

Based on this setup, the reductive quenching of the excited Cr(III) complex by DMA was modelled within the semi-classical Marcus picture of ET. Within Marcus theory,[79–81] electron transfer processes are described based on diabatic potential energy curves (PECs) from a donor (D) to an acceptor state (A), while rare thermal fluctuations of the bath, *e.g.* the solvent environment, lead to structural changes of the reactants which may result in electron transfer in the vicinity of the crossing between the two diabatic PECs. This way, the rate constant for a electron transfer process (k_{ET}) at a given temperature (T) is provided by the driving force or Gibbs free energy (ΔG_0) and the reorganization energy (λ; comprising inner and outer sphere contributions). Furthermore, the electronic communication between the donor and the acceptor state is given by the potential coupling between the two diabatic states (V_{DA}). Further information regarding the utilized semi-classical Marcus picture are provided in the computational details of the SI (section "Intermolecular Electron Transfer" and in particular eqn (11)). Previously, this methodology was utilized and evaluated against (dissipative) quantum dynamical simulations within our group to model light-driven intramolecular electron transfer events in various transition metal complexes[82–84] and photocatalysts[85–87] as well as in the context of redox-active organic batteries.[88,89]

In the present contribution, we extend our computational approach to intermolecular ET reactions, while the electron donor state is defined by $[Cr(dqp)_2]^{3+}$ within its lowest energy doublet state in combination with a non-oxidized DMA, see Fig. 6B. Surprisingly, constrained DFT reveals this lowest energy doublet state of the chromium(III) complex as the true spin-flip state (^{2}E; and not a $^2T_1$ state) without the need of applying further, *e.g.*, broken symmetry approaches. In contrast, the acceptor state comprises of a singly reduced chromium complex and a singly oxidized DMA molecule, see Fig. 6C. Within the acceptor state, a Cr(II) complex is predicted, which features the additional electron within one t_{2g} orbital, which leads consequently to a triplet configuration of the d^4 system ($^3T_1$). Notably, partial spin density is also observed in low-lying π^*_{dqp} orbitals of the coordinating dqp ligands. Thus, the reduction event involves mainly the coordination center and the ligand sphere to a lesser extent. Experimentally, the first reduction event in $[Cr(dqp)_2]^{3+}$ was assigned to a ligand-based process.[37] However, there is a constant debate[90,91] regarding the redox chemistry of Cr(III) complexes and the localization of the respective redox events to be either metal-based or ligand-based, which is reflected by the present computational results which associate this reduction to both metal and ligand contributions. In contrast, the electron hole is clearly localized in the formally doubly occupied highest π_{DMA} orbital which combines contributions from its phenyl ring and the lone-pair of the amino

group. In addition, and less prominently, the chloride ions (p_{Cl}) also participate as partial donors, see Fig. 6C.

Based the donor and acceptor states (Fig. 6B and C), the potential energy landscape was sampled by means of AIMD simulations in the vicinity of their previously relaxed equilibrium structures. Thereby, the relaxed donor structure represents the encounter complex involving the photoexcited Cr(III) complex and the DMA donor in explicit solvent environment. Structurally, this encounter complex is characterized by a pre-orientation of the DMA molecule along the aromatic plane of one dqp ligand in an almost linear configuration. Notably, the amino group of DMA is pointing away from the metal center, while the shortest interatomic distance of merely 1.84 Å is predicted between the donor and the acceptor molecules or d_{Cr-N} = 12.53 Å between the chromium atom and the (amino)-nitrogen of DMA. Within the acceptor state geometry, a slight rotation of the oxidized DMA radical ($DMA^{+\bullet}$) with respect to the Cr complex is observed. In consequence, the distance between the chromium atom and the amino group (N atom) – mainly involved in the oxidation – decreases slightly to ~11.7 Å due to electrostatic effects, while the shortest interatomic distance remains with 2.19 Å almost unchanged. All structural properties and videos based on the AIMD runs are available *via* Zenodo.[92]

During the data processing and the construction of the Marcus parabolas, we followed the histogram approach proposed by Warshel,[93,94] which defines the vertical energy gap (ΔE) between the donor and the acceptor state as the reaction coordinate. Both probability distributions of the energy gap (Fig. 6D), *i.e.* for the donor and the acceptor equilibria, follow almost ideal Gaussian distributions. Subsequently, we improved the accuracy of the Marcus parabola fitting by using the linear response approximation, see eqn (9) the SI.[94–98] This allows for the generation of twice as many points on the two free energy curves without performing additional simulations, see Fig. 6E. Consequently, two identical reorganization energies $\lambda_D = \lambda_A = 1.46$ eV as well as a negative driving force $\Delta G_0 = -0.31$ eV were obtained. Furthermore, the electronic communication as rationalized by means of the potential coupling $V_{DA} = 1.46 \times 10^{-3}$ eV for the (diabatic) donor-acceptor pair was obtained by the energy splitting method.[82,83,85,87] The coupling was obtained based on the switching of states along the AIMD run (Fig. 6F). Finally, the intermolecular ET rate was calculated *via* semi-classical Marcus theory; detailed information regarding the data processing and the conceptional background are provided in the SI, *i.e.* eqn (11). Based on the low temperature as utilized in the AIMD simulations ($T = 100$ K) a very slow intermolecular ET rate of 1.97×10^{-1} s^{-1} is obtained. Experimentally, the bimolecular ET kinetics between the excited $[Cr(dqp)_2]^{3+}$ complex and the DMA donor were studied *via* electrochemical investigations as well as luminescence experiments and subsequent Stern–Volmer analysis. Based on the experimental driving force of approximately −0.41 eV, a quenching rate of 8.3×10^9 M^{-1} s^{-1} was obtained at room temperature (293 K) in acetonitrile for the pseudo-first-order reaction.[36]

Thus, our DFT-predicted driving force −0.31 eV (at $T = 100$ K) is in good agreement with the electrochemically obtained value of −0.41 eV. Therefore, we recalculated our ET rate at a temperature of 293 K and based on the DMA concentration within our periodic box (59.7 × 47.7 × 52.1 $Å^3$, see Fig. 6A), which yields a pseudo-first-order rate constant of 3.41×10^8 M^{-1} s^{-1}. Notably, the driving force is formally temperature-dependent. However, only slight structural changes are predicted between the equilibrated donor and acceptor state (Fig. 6B and C). Thus, the impact of the entropic term and, therefore, temperature-dependency of the ΔG is expected to be negligible. Therefore, both the computational modelling and the experimental findings reveal efficient light-induced reductive quenching of the Cr(III) chromophore by DMA while the ET is fast with respect to the excited state lifetime of $[Cr(dqp)_2]^{3+}$. The difference between the theoretical and the Stern–Volmer-based ET rate of approximately one order of magnitude is mainly a consequence of the intrinsic challenges of density functional theory to describe the complicated electronic structure of $[Cr(dqp)_2]^{3+}$ and especially its low-lying doublet excited states, *i.e.* ^2E *vs.* $^2T_1$, correctly, which leads to an underestimation of the driving force by 0.1 eV. Furthermore, the counter ion was changed from PF_6^- to the smaller Cl^- in the computational modelling.

4 Conclusions

The present computational study carefully evaluates the excited states involved in spin-flip luminescence of a Cr(III) complex, *i.e.* $[Cr(dqp)_2]^{3+}$, as well as its photoredox chemistry in combination with a reductive quencher as previously investigated experimentally.[36] The present computational contribution allows one to rationalize the intramolecular light-driven processes associated with spin-flip phenomena in d^3-based transition metal complexes as well as utilizing these millisecond-lived excited states in photoredox chemistry. Such findings are of significance for the development of efficient noble-metal free photocatalysts.

The excited-state landscape at the Franck–Condon point was carefully assessed by state-of-the-art multiconfigurational simulations which account for both static and dynamic electron correlation. These MS-RASPT2//RASSCF results were utilized to evaluate the performance of cost-efficient TDDFT simulations to describe the complex electronic structure of such a molecular ruby and the respective light-driven processes, *i.e.*, associated with its ligand field based transitions ($^4A_2 \rightarrow {}^4T_2$ and $^4A_2 \rightarrow {}^4T_1$). Subsequently, our computational focus was set on evaluating the spin-flip phenomenon and the underlying thermodynamics as well as the kinetics of various intersystem crossing pathways, which lead eventually to the population of millisecond-lived doublet states. Based on the present MS-RASPT2 results, ultrafast ISC leads within sub-ps to few picoseconds to an almost identical population of the quasi-isoenergetic ^2E and $^2T_1$ states (Fig. 4). Finally, the emission of the present molecular ruby is mostly associated with the slightly shorter-lived ^2E states.

Subsequently, the focus of our computational investigation was set beyond the description of the photophysical properties and the mechanistic understanding of the spin-flip phenomena in Cr(III) complexes, namely on harvesting these extraordinarily

long-lived excited states in photoredox processes. To this aim, *ab initio* molecular dynamics simulations were carried out to investigate the photoinduced reductive quenching of an excited $[Cr(dqp)_2]^{3+}$, by an organic donor, *i.e.* *N*,*N*-dimethylaniline (DMA),[36] as investigated previously based on electrochemical and luminescence and transient absorption experiments as well as subsequent Stern–Volmer analysis. These simulations allowed the structural configuration of the encounter complex (in acetonitrile solution) to be assessed and for the electronic structure of the redox intermediates associated with the intermolecular electron transfer to be elucidated. Based on our simulations the reduction of the chromium complexes is mostly metal-based and leads to a d^4 triplet configuration, while only a minor electron density contribution is transferred from the highest energy π_{DMA} orbital the π^* orbitals of the dqp ligands. Finally, the thermodynamics and kinetics of the light-driven intermolecular electron transfer were investigated within the semi-classical Marcus picture. Based on our computational modelling, a driving force of −0.31 eV and a reorganization energy 1.46 eV – which involves both inner and outer sphere contributions – was predicted, which is in good agreement with electrochemical results. Based on these results an ET rate of 3.41×10^8 M^{-1} s^{-1} was obtained for the pseudo-first order excited state quenching reaction, which is particularly fast for typically weakly coupled intermolecular transfer processes. This rate constant as rationalized by AIMD simulations is in good agreement with the experimental Stern–Volmer kinetics, which predict an even slightly faster reductive quenching of the excited chromium complex.

Therefore, the insights at the molecular level presented herein will contribute to the transformation from noble metal-based photocatalysis to efficient noble metal-free photocatalysts.

Author contributions

The project was supervised and coordinated by S. Kupfer, in consultation with O. Wenger. G. Yang performed all computational simulations and was the primary contributor to writing the manuscript, aided by S. Kupfer and G. Shillito. P. Seeber guided the setup and analysis of the AIMD simulations. All authors contributed to editing of the manuscript.

Conflicts of interest

There are no conflicts to declare.

Data availability

All optimized structures, high resolution images and trajectories are available *via* the free online repository Zenodo (DOI: https://doi.org/10.5281/zenodo.15849517).[92]

The data supporting this article have been included in the main manuscript as well as in the SI.

Supplementary information: computational details (geometry optimization, ground and excited state properties within the Franck–Condon region, setup of multiconfigurational simulations, intermolecular electron transfer kinetics and AIMD setup), simulated UV-vis spectra, Marcus parabolas, excited state properties and composition. See DOI: https://doi.org/10.1039/d5sc05170c.

Acknowledgements

Financial support by the Deutsche Forschungsgemeinschaft (DFG, German Research Foundation) – project numbers 456209398 and 448713509 as well as project number 364549901, TRR 234 [A4] – is gratefully acknowledged. All calculations were performed at the Universitätsrechenzentrum of the Friedrich-Schiller University Jena.

References

1 J. Demas, E. Harris and R. McBride, Energy transfer from luminescent transition metal complexes to oxygen, *J. Am. Chem. Soc.*, 1977, **99**, 3547–3551.
2 Y. Gil, R. C. de Santana, A. S. S. de Camargo, L. G. Merízio, P. F. Carreño, P. Fuentealba, J. Manzur and E. Spodine, Dual visible and near-infrared luminescence in mononuclear macrocyclic erbium (III) complexes via ligand and metal centred excitation, *Dalton Trans.*, 2023, **52**, 3158–3168.
3 F. Glaser and O. S. Wenger, Recent progress in the development of transition-metal based photoredox catalysts, *Coord. Chem. Rev.*, 2020, **405**, 213129.
4 L. C.-C. Lee and K. K.-W. Lo, Luminescent and photofunctional transition metal complexes: From molecular design to diagnostic and therapeutic applications, *J. Am. Chem. Soc.*, 2022, **144**, 14420–14440.
5 C. Wegeberg and O. S. Wenger, Luminescent first-row transition metal complexes, *JACS Au*, 2021, **1**, 1860–1876.
6 O. S. Wenger, Proton-Coupled Electron Transfer Originating from Excited States of Luminescent Transition-Metal Complexes, *Eur. J. Chem.*, 2011, **17**, 11692–11702.
7 V. W.-W. Yam, A. K.-W. Chan and E. Y.-H. Hong, Charge-transfer processes in metal complexes enable luminescence and memory functions, *Nat. Rev. Chem.*, 2020, **4**, 528–541.
8 Y. Zhang, T. S. Lee, J. M. Favale, D. C. Leary, J. L. Petersen, G. D. Scholes, F. N. Castellano and C. Milsmann, Delayed fluorescence from a zirconium (IV) photosensitizer with ligand-to-metal charge-transfer excited states, *Nat. Chem.*, 2020, **12**, 345–352.
9 E. Sakuda, Y. Ando, A. Ito and N. Kitamura, Long-lived and temperature-independent emission from a novel ruthenium (II) complex having an arylborane charge-transfer unit, *Inorg. Chem.*, 2011, **50**, 1603–1613.
10 X. Yan, J. Xue and Y. Wang, Synthesis and theoretical and photophysical study on a series of neutral ruthenium (II) complexes with donor–metal–accepter configuration, *Inorg. Chem.*, 2023, **62**, 1476–1487.
11 H. Amouri, Luminescent complexes of platinum, iridium, and coinage metals containing N-heterocyclic carbene

ligands: design, structural diversity, and photophysical properties, *Chem. Rev.*, 2022, **123**, 230–270.

12 P. Anuja and P. Paira, Luminescent anticancer Ru (II)-arenebipyridine and phenanthroline complexes: Synthesis, characterization, DFT studies, biological interactions and cellular imaging application, *J. Inorg. Biochem.*, 2020, **208**, 111099.

13 S. Cerfontaine, L. Troian-Gautier, S. A. Wehlin, F. Loiseau, E. Cauët and B. Elias, Tuning the excited-state deactivation pathways of dinuclear ruthenium (II) 2, 2′-bipyridine complexes through bridging ligand design, *Dalton Trans.*, 2020, **49**, 8096–8106.

14 Y. Chi and P.-T. Chou, Contemporary progresses on neutral, highly emissive Os (II) and Ru (II) complexes, *Chem. Soc. Rev.*, 2007, **36**, 1421–1431.

15 J. Li, K. Chen, J. Wei, Y. Ma, R. Zhou, S. Liu, Q. Zhao and W.-Y. Wong, Reversible on–off switching of excitation-wavelength-dependent emission of a phosphorescent soft salt based on platinum (II) complexes, *J. Am. Chem. Soc.*, 2021, **143**, 18317–18324.

16 D. Maity, C. Bhaumik, D. Mondal and S. Baitalik, Photoinduced intramolecular energy transfer and anion sensing studies of isomeric Ru II Os II complexes derived from an asymmetric phenanthroline–terpyridine bridge, *Dalton Trans.*, 2014, **43**, 1829–1845.

17 F. Monti, A. Baschieri, L. Sambri and N. Armaroli, Excited-state engineering in heteroleptic ionic iridium (III) complexes, *Acc. Chem. Res.*, 2021, **54**, 1492–1505.

18 M. T. Rupp, N. Shevchenko, G. S. Hanan and D. G. Kurth, Enhancing the photophysical properties of Ru (II) complexes by specific design of tridentate ligands, *Coord. Chem. Rev.*, 2021, **446**, 214127.

19 M. Z. Shafikov, A. V. Zaytsev and V. N. Kozhevnikov, Halide-enhanced spin–orbit coupling and the phosphorescence rate in Ir (III) complexes, *Inorg. Chem.*, 2021, **60**, 642–650.

20 S. Yoon and T. S. Teets, Red to near-infrared phosphorescent Ir (III) complexes with electron-rich chelating ligands, *Chem. Commun.*, 2021, **57**, 1975–1988.

21 M. Yoshida and M. Kato, Cation-controlled luminescence behavior of anionic cyclometalated platinum (II) complexes, *Coord. Chem. Rev.*, 2020, **408**, 213194.

22 F. Zhou, M. Gu and Y. Chi, Azolate-Based Osmium (II) Complexes with Luminescence Spanning Visible and Near Infrared Region, *Eur. J. Inorg. Chem.*, 2022, **2022**, e202200222.

23 S. K. Seth and P. Purkayastha, Unusually large singlet oxygen (1O2) production by very weakly emissive pyrene-functionalized iridium (III) complex: Interplay between excited 3ILCT/3IL and 3MLCT states, *Eur. J. Inorg. Chem.*, 2020, **2020**, 2990–2997.

24 J. D. Braun, I. B. Lozada, C. Kolodziej, C. Burda, K. M. Newman, J. van Lierop, R. L. Davis and D. E. Herbert, Iron (II) coordination complexes with panchromatic absorption and nanosecond charge-transfer excited state lifetimes, *Nat. Chem.*, 2019, **11**, 1144–1150.

25 P. Dierks, A. Päpcke, O. S. Bokareva, B. r. Altenburger, T. Reuter, K. Heinze, O. Kühn, S. Lochbrunner and M. Bauer, Ground-and excited-state properties of iron (II) complexes linked to organic chromophores, *Inorg. Chem.*, 2020, **59**, 14746–14761.

26 T. Reuter, A. Kruse, R. Schoch, S. Lochbrunner, M. Bauer and K. Heinze, Higher MLCT lifetime of carbene iron (II) complexes by chelate ring expansion, *Chem. Commun.*, 2021, **57**, 7541–7544.

27 A. Ghosh, J. T. Yarranton and J. K. McCusker, Establishing the origin of Marcus-inverted-region behaviour in the excited-state dynamics of cobalt (III) polypyridyl complexes, *Nat. Chem.*, 2024, **16**, 1665–1672.

28 A. Y. Chan, A. Ghosh, J. T. Yarranton, J. Twilton, J. Jin, D. M. Arias-Rotondo, H. A. Sakai, J. K. McCusker and D. W. MacMillan, Exploiting the Marcus inverted region for first-row transition metal–based photoredox catalysis, *Science*, 2023, **382**, 191–197.

29 J. K. McCusker, Electronic structure in the transition metal block and its implications for light harvesting, *Science*, 2019, **363**, 484–488.

30 W. R. Kitzmann, J. Moll and K. Heinze, Spin-flip luminescence, *Photochem. Photobiol. Sci.*, 2022, **21**, 1309–1331.

31 W. R. Kitzmann and K. Heinze, Charge-transfer and spin-flip states: Thriving as complements, *Angew. Chem.*, 2023, **62**, e202213207.

32 N. Sinha, P. Yaltseva and O. S. Wenger, The Nephelauxetic Effect Becomes an Important Design Factor for Photoactive First-Row Transition Metal Complexes, *Angew. Chem.*, 2023, **62**, e202303864.

33 J.-R. Jiménez, B. Doistau, C. Besnard and C. Piguet, Versatile heteroleptic bis-terdentate Cr (III) chromophores displaying room temperature millisecond excited state lifetimes, *Chem. Commun.*, 2018, **54**, 13228–13231.

34 A. Kirk and G. B. Porter, Luminescence of chromium (III) complexes, *J. Phys. Chem.*, 1980, **84**, 887–891.

35 S. Otto, M. Dorn, C. Förster, M. Bauer, M. Seitz and K. Heinze, Understanding and exploiting long-lived near-infrared emission of a molecular ruby, *Coord. Chem. Rev.*, 2018, **359**, 102–111.

36 T. H. Burgin, F. Glaser and O. S. Wenger, Shedding light on the oxidizing properties of spin-flip excited states in a CrIII polypyridine complex and their use in photoredox catalysis, *J. Am. Chem. Soc.*, 2022, **144**, 14181–14194.

37 J.-R. n. Jiménez, B. Doistau, C. M. Cruz, C. l. Besnard, J. M. Cuerva, A. G. Campaña and C. Piguet, Chiral molecular ruby [Cr (dqp) 2] 3+ with long-lived circularly polarized luminescence, *J. Am. Chem. Soc.*, 2019, **141**, 13244–13252.

38 J. R. Jiménez, M. Poncet, S. Míguez-Lago, S. Grass, J. Lacour, C. Besnard, J. M. Cuerva, A. G. Campaña and C. Piguet, Bright Long-Lived Circularly Polarized Luminescence in Chiral Chromium (III) Complexes, *Angew. Chem.*, 2021, **60**, 10095–10102.

39 S. Otto, M. Grabolle, C. Förster, C. Kreitner, U. Resch-Genger and K. Heinze, [Cr (ddpd) 2] 3+: A Molecular, Water-Soluble, Highly NIR-Emissive Ruby Analogue, *Angew. Chem.*, 2015, **54**, 11572–11576.

40 N. Sinha, J. R. Jiménez, B. Pfund, A. Prescimone, C. Piguet and O. S. Wenger, A Near-Infrared-II Emissive Chromium (III) Complex, *Angew. Chem.*, 2021, **133**, 23915–23921.

41 J.-R. Jiménez, B. Doistau, C. M. Cruz, C. Besnard, J. M. Cuerva, A. G. Campaña and C. Piguet, Chiral molecular ruby [Cr (dqp) 2] 3+ with long-lived circularly polarized luminescence, *J. Am. Chem. Soc.*, 2019, **141**, 13244–13252.

42 K. D. Barker, K. A. Barnett, S. M. Connell, J. W. Glaeser, A. J. Wallace, J. Wildsmith, B. J. Herbert, J. F. Wheeler and N. A. Kane-Maguire, Synthesis and characterization of heteroleptic Cr (diimine) 3 3+ complexes, *Inorg. Chim. Acta*, 2001, **316**, 41–49.

43 B. Doistau, G. Collet, E. A. Bolomey, V. Sadat-Noorbakhsh, C. Besnard and C. Piguet, Heteroleptic ter–bidentate Cr (III) complexes as tunable optical sensitizers, *Inorg. Chem.*, 2018, **57**, 14362–14373.

44 N. Serpone, M. Jamieson, M. Henry, M. Hoffman, F. Bolletta and M. Maestri, Excited-state behavior of polypyridyl complexes of chromium (III), *J. Am. Chem. Soc.*, 1979, **101**, 2907–2916.

45 F. Reichenauer, C. Wang, C. Förster, P. Boden, N. Ugur, R. Báez-Cruz, J. Kalmbach, L. M. Carrella, E. Rentschler, C. Ramanan, G. Niedner-Schatteburg, M. Gerhards, M. Seitz, U. Resch-Genger and K. Heinze, Strongly Red-Emissive Molecular Ruby [Cr(bpmp)2]3+ Surpasses [Ru(bpy)3]2+, *J. Am. Chem. Soc.*, 2021, **143**, 11843–11855.

46 A. König, R. Naumann, C. Förster, J. Klett and K. Heinze, A Near-Infrared-II Luminescent and Photoactive Vanadium (II) Complex with a 760 ns Excited State Lifetime, *J. Am. Chem. Soc.*, 2025, **147**, 20833–20842.

47 N. R. East, R. Naumann, C. Förster, C. Ramanan, G. Diezemann and K. Heinze, Oxidative two-state photoreactivity of a manganese (IV) complex using near-infrared light, *Nat. Chem.*, 2024, **16**, 827–834.

48 J. P. Harris, C. Reber, H. E. Colmer, T. A. Jackson, A. P. Forshaw, J. M. Smith, R. A. Kinney and J. Telser, Near-infrared 2Eg→ 4A2g and visible LMCT luminescence from a molecular bis-(tris (carbene) borate) manganese (IV) complex, *Can. J. Chem.*, 2017, **95**, 547–552.

49 R. Ham, C. J. Nielsen, S. Pullen and J. N. Reek, Supramolecular coordination cages for artificial photosynthesis and synthetic photocatalysis, *Chem. Rev.*, 2023, **123**, 5225–5261.

50 D. Escudero and L. González, Raspt2/rasscf vs range-separated/hybrid dft methods: Assessing the excited states of a ru (ii) bipyridyl complex, *J. Chem. Theory Comput.*, 2012, **8**, 203–213.

51 V. Sauri, L. Serrano-Andrés, A. R. M. Shahi, L. Gagliardi, S. Vancoillie and K. Pierloot, Multiconfigurational second-order perturbation theory restricted active space (RASPT2) method for electronic excited states: A benchmark study, *J. Chem. Theory Comput.*, 2011, **7**, 153–168.

52 K. M. Ziems, S. Gräfe and S. Kupfer, Photo-Induced Charge Separation vs. Degradation of a BODIPY-Based Photosensitizer Assessed by TDDFT and RASPT2, *Catalysts*, 2018, **8**, 520.

53 M. J. Frisch, G. W. Trucks, H. B. Schlegel, G. E. Scuseria, M. A. Robb, J. R. Cheeseman, G. Scalmani, V. Barone, G. A. Petersson, H. Nakatsuji, X. Li, M. Caricato, A. V. Marenich, J. Bloino, B. G. Janesko, R. Gomperts, B. Mennucci, H. P. Hratchian, J. V. Ortiz, A. F. Izmaylov, J. L. Sonnenberg, D. Williams-Young, F. Ding, F. Lipparini, F. Egidi, J. Goings, B. Peng, A. Petrone, T. Henderson, D. Ranasinghe, V. G. Zakrzewski, J. Gao, N. Rega, G. Zheng, W. Liang, M. Hada, M. Ehara, K. Toyota, R. Fukuda, J. Hasegawa, M. Ishida, T. Nakajima, Y. Honda, O. Kitao, H. Nakai, T. Vreven, K. Throssell, J. A. Montgomery Jr, J. E. Peralta, F. Ogliaro, M. J. Bearpark, J. J. Heyd, E. N. Brothers, K. N. Kudin, V. N. Staroverov, T. A. Keith, R. Kobayashi, J. Normand, K. Raghavachari, A. P. Rendell, J. C. Burant, S. S. Iyengar, J. Tomasi, M. Cossi, J. M. Millam, M. Klene, C. Adamo, R. Cammi, J. W. Ochterski, R. L. Martin, K. Morokuma, O. Farkas, J. B. Foresman and D. J. Fox, *Gaussian 16 Rev. C.01*, 2016.

54 A. D. Beck, Density-functional thermochemistry. III. The role of exact exchange, *J. Chem. Phys.*, 1993, **98**, 5648–5652.

55 A. D. Becke, Density-functional exchange-energy approximation with correct asymptotic behavior, *Phys. Rev. A*, 1988, **38**, 3098.

56 J. Guthmuller and L. González, Simulation of the resonance Raman intensities of a ruthenium–palladium photocatalyst by time dependent density functional theory, *Phys. Chem. Chem. Phys.*, 2010, **12**, 14812–14821.

57 C. Lee, W. Yang and R. G. Parr, Development of the Colle-Salvetti correlation-energy formula into a functional of the electron density, *Phys. Rev. B*, 1988, **37**, 785.

58 G. E. Shillito, T. B. J. Hall, D. Preston, P. Traber, L. Wu, K. E. A. Reynolds, R. Horvath, X. Z. Sun, N. T. Lucas, J. D. Crowley, M. W. George, S. Kupfer and K. C. Gordon, Dramatic Alteration of ^{3}ILCT Lifetimes Using Ancillary Ligands in $[Re(L)(CO)_3(phen\text{-}TPA)]^{n+}$ Complexes: An Integrated Spectroscopic and Theoretical Study, *J. Am. Chem. Soc.*, 2018, **140**, 4534–4542.

59 G. E. Shillito, D. Preston, P. Traber, J. Steinmetzer, C. J. McAdam, J. D. Crowley, P. Wagner, S. Kupfer and K. C. Gordon, Excited-state switching frustrates the tuning of properties in triphenylamine-donor-ligand rhenium (I) and platinum (II) complexes, *Inorg. Chem.*, 2020, **59**, 6736–6746.

60 F. Aquilante, J. Autschbach, R. K. Carlson, L. F. Chibotaru, M. G. Delcey, L. De Vico, I. F. Galván, N. Ferré, L. M. Frutos, L. Gagliardi, M. Garavelli, A. Giussani, C. E. Hoyer, G. Li Manni, H. Lischka, D. Ma, P. Å. Malmqvist, T. Müller, A. Nenov, M. Olivucci, T. B. Pedersen, D. Peng, F. Plasser, B. Pritchard, M. Reiher, I. Rivalta, I. Schapiro, J. Segarra-Martí, M. Stenrup, D. G. Truhlar, L. Ungur, A. Valentini, S. Vancoillie, V. Veryazov, V. P. Vysotskiy, O. Weingart, F. Zapata and R. Lindh, Molcas 8: New capabilities for multiconfigurational quantum chemical calculations across the periodic table, *J. Comput. Chem.*, 2016, **37**, 506–541.

61 J. Hutter, M. Iannuzzi, F. Schiffmann and J. VandeVondele, cp2k: atomistic simulations of condensed matter systems, *Wiley Interdiscip. Rev.: Comput. Mol. Sci.*, 2014, **4**, 15–25.
62 J. VandeVondele, M. Krack, F. Mohamed, M. Parrinello, T. Chassaing and J. Hutter, Quickstep: Fast and accurate density functional calculations using a mixed Gaussian and plane waves approach, *Comput. Phys. Commun.*, 2005, **167**, 103–128.
63 B. Miehlich, A. Savin, H. Stoll and H. Preuss, Results obtained with the correlation energy density functionals of becke and Lee, Yang and Parr, *Chem. Phys. Lett.*, 1989, **157**, 200–206.
64 P. M. Becker, C. Förster, L. M. Carrella, P. Boden, D. Hunger, J. van Slageren, M. Gerhards, E. Rentschler and K. Heinze, Spin Crossover and Long-Lived Excited States in a Reduced Molecular Ruby, *Eur. J. Chem.*, 2020, **26**, 7199–7204.
65 W. R. Kitzmann, C. Ramanan, R. Naumann and K. Heinze, Molecular ruby: exploring the excited state landscape, *Dalton Trans.*, 2022, **51**, 6519–6525.
66 R. W. Jones, A. J. Auty, G. Wu, P. Persson, M. V. Appleby, D. Chekulaev, C. R. Rice, J. A. Weinstein, P. I. Elliott and P. A. Scattergood, Direct determination of the rate of intersystem crossing in a near-IR luminescent Cr (III) triazolyl complex, *J. Am. Chem. Soc.*, 2023, **145**, 12081–12092.
67 J. N. Schrauben, K. L. Dillman, W. F. Beck and J. K. McCusker, Vibrational coherence in the excited state dynamics of Cr (acac) 3: probing the reaction coordinate for ultrafast intersystem crossing, *Chem. Sci.*, 2010, **1**, 405–410.
68 Y. Ye, M. Poncet, P. Yaltseva, P. Salcedo-Abraira, A. Rodríguez-Diéguez, J. H. Martín, L. Cuevas-Contreras, C. M. Cruz, B. Doistau and C. Piguet, Modulating the spin–flip rates and emission energies through ligand design in chromium (iii) molecular rubies, *Chem. Sci.*, 2025, **16**, 5205–5213.
69 M. Reiher, Relativistic douglas–kroll–hess theory, *Wiley Interdiscip. Rev.:Comput. Mol. Sci.*, 2012, **2**, 139–149.
70 N. A. P. Kane-Maguire, in *Photochemistry and Photophysics of Coordination Compounds I*, ed. V. Balzani and S. Campagna, Springer Berlin, Heidelberg, 1st edn, 2007, vol. 1, ch. 2, pp. 37–67.
71 C. Wang, H. Li, T. H. Bürgin and O. S. Wenger, Cage escape governs photoredox reaction rates and quantum yields, *Nat. Chem.*, 2024, **16**, 1151–1159.
72 B. Miehlich, A. Savin, H. Stoll and H. Preuss, Results obtained with the correlation energy density functionals of Becke and Lee, Yang and Parr, *Chem. Phys. Lett.*, 1989, **157**, 200–206.
73 J. VandeVondele and J. Hutter, Gaussian basis sets for accurate calculations on molecular systems in gas and condensed phases, *J. Chem. Phys.*, 2007, **127**, 114105.
74 S. Grimme, S. Ehrlich and L. Goerigk, Effect of the damping function in dispersion corrected density functional theory, *J. Comput. Chem.*, 2011, **32**, 1456–1465.
75 J. Wang, R. M. Wolf, J. W. Caldwell, P. A. Kollman and D. A. Case, Development and testing of a general amber force field, *J. Comput. Chem.*, 2004, **25**, 1157–1174.
76 X. He, V. H. Man, W. Yang, T.-S. Lee and J. Wang, A fast and high-quality charge model for the next generation general AMBER force field, *J. Chem. Phys.*, 2020, **153**, 114502.
77 J. Wang, W. Wang, P. A. Kollman and D. A. Case, Automatic atom type and bond type perception in molecular mechanical calculations, *J. Mol. Graphics Modell.*, 2006, **25**, 247–260.
78 W. D. Cornell, P. Cieplak, C. I. Bayly, I. R. Gould, K. M. Merz, D. M. Ferguson, D. C. Spellmeyer, T. Fox, J. W. Caldwell and P. A. Kollman, A second generation force field for the simulation of proteins, nucleic acids, and organic molecules, *J. Am. Chem. Soc.*, 1995, **117**, 5179–5197.
79 R. A. Marcus, On the theory of oxidation-reduction reactions involving electron transfer. I, *J. Chem. Phys.*, 1956, **24**, 966–978.
80 R. A. Marcus, On the theory of electron-transfer reactions. VI. Unified treatment for homogeneous and electrode reactions, *J. Chem. Phys.*, 1965, **43**, 679–701.
81 R. A. Marcus, Electron transfer reactions in chemistry: theory and experiment (Nobel lecture), *Angew Chem. Int. Ed. Engl.*, 1993, **32**, 1111–1121.
82 A. Koch, D. Kinzel, F. Dröge, S. Gräfe and S. Kupfer, Photochemistry and Electron Transfer Kinetics in a Photocatalyst Model Assessed by Marcus Theory and Quantum Dynamics, *J. Phys. Chem. C*, 2017, **121**, 16066–16078.
83 G. Yang, G. E. Shillito, C. Zens, B. Dietzek-Ivanšić and S. Kupfer, The three kingdoms—Photoinduced electron transfer cascades controlled by electronic couplings, *J. Chem. Phys.*, 2023, **159**, 024109.
84 G. Yang, L. Blechschmidt, L. Zedler, C. Zens, K. Witas, M. Schmidt, B. Esser, S. Rau, G. E. Shillito, B. Dietzek-Ivanšić and S. Kupfer, Excited State Branching Processes in a Ru(II)-Based Donor–Acceptor–Donor System, *Chem.–Eur. J.*, 2025, **31**, e202404671.
85 M. Staniszewska, S. Kupfer and J. Guthmuller, Theoretical investigation of the electron-transfer dynamics and photodegradation pathways in a hydrogen-evolving ruthenium–palladium photocatalyst, *Eur. J. Chem.*, 2018, **24**, 11166–11176.
86 G. E. Shillito, S. Rau and S. Kupfer, Plugging the 3MC sink in RuII-Based photocatalysts, *ChemCatChem*, 2023, **15**, e202201489.
87 M. Staniszewska, S. Kupfer and J. Guthmuller, Effect of the catalytic center on the electron transfer dynamics in hydrogen-evolving ruthenium-based photocatalysts investigated by theoretical calculations, *J. Phys. Chem. C*, 2019, **123**, 16003–16013.
88 C. Zens, C. Friebe, U. S. Schubert, M. Richter and S. Kupfer, Tailored charge transfer kinetics in precursors for organic radical batteries: A joint synthetic-theoretical approach, *ChemSusChem*, 2023, **16**, e202201679.
89 S. Mitra, C. Zens, S. Kupfer and D. Diddens, Toward robust electronic coupling predictions in redox-active TEMPO/TEMPO+ systems, *J. Chem. Phys.*, 2024, **161**, 214106.
90 C. Scarborough, S. Sproules, T. Weyermuller, S. DeBeer and K. Wieghardt, *Electronic and Molecular Structures of the*

Members of the Electron Transfer Series, SLAC National Accelerator Lab, Menlo Park, CA (United States), 2013.

91 C. C. Scarborough, K. M. Lancaster, S. DeBeer, T. Weyhermüller, S. Sproules and K. Wieghardt, Experimental fingerprints for redox-active terpyridine in [Cr (tpy) 2](PF6) n (n= 3–0), and the remarkable electronic structure of [Cr (tpy) 2] 1, *Inorg. Chem.*, 2012, **51**, 3718–3732.

92 G. Yang, *Structural properties of Cr[(dqp)2]3+*, Zenodo, 2025, DOI: **10.5281/zenodo.15849517**.

93 G. King and A. Warshel, Investigation of the free energy functions for electron transfer reactions, *J. Chem. Phys.*, 1990, **93**, 8682–8692.

94 A. Warshel, Dynamics of reactions in polar solvents. Semiclassical trajectory studies of electron-transfer and proton-transfer reactions, *J. Phys. Chem.*, 1982, **86**, 2218–2224.

95 L. Hu, M. Farrokhnia, J. Heimdal, S. Shleev, L. Rulisek and U. Ryde, Reorganization energy for internal electron transfer in multicopper oxidases, *J. Phys. Chem. B*, 2011, **115**, 13111–13126.

96 J. Blumberger, Free energies for biological electron transfer from QM/MM calculation: method, application and critical assessment, *Phys. Chem. Chem. Phys.*, 2008, **10**, 5651–5667.

97 J. Blumberger and M. Sprik, Quantum versus classical electron transfer energy as reaction coordinate for the aqueous Ru2+/Ru3+ redox reaction, *Theor. Chem. Acc.*, 2006, **115**, 113–126.

98 M. Tachiya, Relation between the electron-transfer rate and the free energy change of reaction, *J. Phys. Chem.*, 1989, **93**, 7050–7052.